Exploratory Tests on a Biaxial Compression Hopkinson Bar Set-up

Bastien Durand, Pierre Quillery, Ahmed Zouari, Han Zhao

EXPLORATORY TESTS ON A BIAXIAL COMPRESSION HOPKINSON BAR SET-UP

B. Durand (bastien.durand@ens-paris-saclay.fr)[1], P. Quillery[1], A. Zouari[2], H. Zhao[1,3]

[1]Université Paris-Saclay, ENS Paris-Saclay, CNRS, LMT - Laboratoire de Mécanique et Technologie, 91190, Gif-sur-Yvette, France

[2]MINES ParisTech, 75006 Paris, France

[3]Sorbonne Universités, UFR 919, 4 Place Jussieu, F-75252 Paris cedex 05

Abstract:

Background: Multiaxial dynamic loadings occur in many industrial cases and multiaxial dynamic test development is thus a crucial issue. Objective: To meet this challenge, a biaxial compression Hopkinson bar set-up is designed. Methods: The set-up consists of a striker, an input bar, an internal output bar and a co-axial external output tube (surrounding the internal bar). The internal output bar measures the axial loading of the cross sample whereas the external output bar measures the transverse one via a mechanism. This mechanism uses two intermediate parts with inclined sliding surfaces. Results: Gauges on the bars enable for force measurements in the set-up, and the sample displacement field is obtained by digital image correlation. Simple compression tests on cuboid samples inserted between the input bar and the internal output bar give the sample material behavior. Then, to determine the friction at the mechanism sliding surfaces, identical samples are inserted between the input bar and the external output bar, and are compressed. Conclusions: Finally, the consistency of the measurements obtained during a biaxial compression test on a cross sample can be checked from the previously measured parameters and from numerical simulations.

Keywords: biaxial compression dynamic test, Hopkinson bars

1 Introduction

Multiaxial dynamic loadings usually occur in many industrial cases such as automotive impacts [1], high-speed forming [2] or high-speed machining [3]. Multiaxial dynamic test development is therefore a crucial issue. Unfortunately, most of the dynamic tests are uniaxial. For instance, the very common Hopkinson bar test (which enables for accurate measurements at high strain rates) uses the uniaxial compression loading generated by the impact of a projectile.

In order to perform multiaxial tests, many set-ups have thus been designed to obtain multiaxial loadings from an initial uniaxial loading device. For example, a radial pressure can be applied to a cylindrical sample mounted on Hopkinson bars thanks to a confinement device. One can use a pressure vessel that enables for a controlled quasi-static pressure to be applied from a fluid [4]. Inserting the cylindrical sample inside a rigid tube can generate a dynamic radial loading even though the ratio between the radial pressure and the axial stress strongly depends on the sample material, in particular on its Poisson's ratio [5]. Using a confinement tube made of a perfect plastic behavior material makes it possible to maintain a constant radial pressure [6]. A rigid confinement can also be imposed to a cruciform sample with a pre-loading system [7].

Another idea is to combine shear and compressive loadings. An inclined shear/compression specimen [8] or pressure bars with beveled ends [9] can be used to apply such combined loadings. The combined torsion-compression Hopkinson bar technique using torsional and compressive bars at each side of specimen was also reported [10]. It can also be carried out by blocking a brake on the input bar and by applying both compression/tension and torsion on the input boundary of the bar. Then the sudden fracture of the brake generates both

torsion and tension/compression waves [11]. Unfortunately, the difference between the wave celerities does not enable simultaneous loadings to be obtained [12].

In order to apply biaxial loadings, two perpendicular Hopkinson bar devices have been built [13]. An explosive is used to obtain simultaneous loadings. The system is rather expensive and difficult to use. Recently, biaxial Hopkinson bar systems using two impactors were reported to generate biaxial compression states on samples [14], but obtaining two simultaneous impacts remains difficult. Another simple way to apply an equi-biaxial loading is the bulge-test using Hopkinson bars described in [15]. In this test, the external boundary of a circular sheet is leant against the tubular boundary of the output bar while the other side of the sheet is submitted to the pressure of a fluid compressed by the input bar. A biaxial tensile state is thus obtained at the center of the sheet. Unfortunately, only sheets can be tested and the displacement field on the sample cannot be easily measured.

From the short review above, it can be seen that the multiaxial testing design is still a tough issue. There are no commonly admitted testing set-ups and the design of such a test depend on the aimed loading state and on specimens. This paper is focused on biaxial compression and a new concept of Hopkinson bar system has been designed and tested. Its principle and its characteristics are described in Section 2. Then, Sections 3 and 4 present respectively the raw experimental results obtained from calibration tests and the analysis of a bi-axial test thanks to numerical simulations.

2 Design of the new set-up

2.1 Set-up characteristics

The designed bi-axial set-up uses a mechanism with intermediate parts with sliding surfaces and a cruciform specimen. This mechanism with sliding surfaces at 45° with respect

to the axial direction was placed between the single input bar, the internal output bar and the co-axial external output tube (Figure 1). After the striker impact on the input bar, the internal output bar measures the axial loading of the cross sample whereas the external output bar (the single tube that surrounds the internal output bar) measures the transversal one via the mechanism.

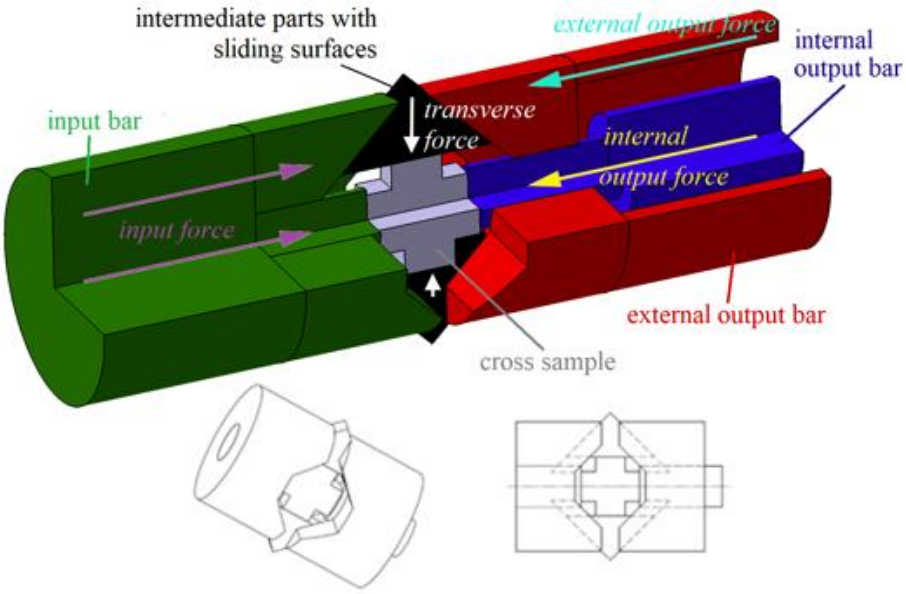

Figure 1: Schematic of the experimental configuration (cut view) with the relative motion of each part and the applied forces (up). Three-dimensional (down, left) and uncut (down, right) views without the three bars.

Using a single loading impulse avoids the difficulty due to non-simultaneous impacts occurring with perpendicular Hopkinson bar devices [13], [14]. Another advantage of such a design lies in the fact that the ratio between the axial and the transverse loadings is imposed by the ratio between the external and the internal output bar impedances and by the sliding surface angle of the mechanism.

The pressure bars are made of steel and their characteristics are given in Table 1. The external and the internal output bars have nearly the same impedance in order to ensure, on an

isotropic sample, an approximate equality between the internal and the external loadings, and therefore between the axial and the transverse loadings, thanks to the mechanism. The difference between the internal radius of the external output bar (R_{ieo}) and the internal output bar radius (R_{io}) is 3 mm, which is sufficient to place the gauges glued on the internal bar and their cables. These electrical cables exit from the external bar at the output end (i.e. at the opposite of the set-up). Nylon bearings are inserted between the two co-axial output bars and some of them are opened (Figure 2g) to let a passage to the cables.

bar	density	wave celerity	radius		length
			external	internal	
striker	ρ_i = 8050 kg.m^{-3}	C_i = 4600 m.s^{-1}	R_i = 11 mm		1.25 m
input					4 m
internal output	ρ_{io} = 7800 kg.m^{-3}	C_{io} = 5100 m.s^{-1}	R_{io} = 6 mm		2 m
external output	ρ_{eo} = 7400 kg.m^{-3}	C_{eo} = 5200 m.s^{-1}	R_{eeo} = 11 mm	R_{ieo} = 9 mm	2 m

Table 1: Mass densities, tensile-compressive wave celerities, radii and lengths of the bars.

The detailed drawings of the set-up parts are given in Figure 2. The sample size (boundary to boundary) is 10 mm × 10 mm and its thickness is 5 mm (Figure 2e). The shape of the parts with the two sliding surfaces (noted “a” in Figure 2) has been chosen to maximize the stiffness. One of this part (the left-hand one in Figure 1, in green) is inserted between the input bar and the two transverse triangular parts (noted “d”) and the other (the right-hand one in Figure 1, in red) is inserted between the two transverse triangular parts and the external output bar.

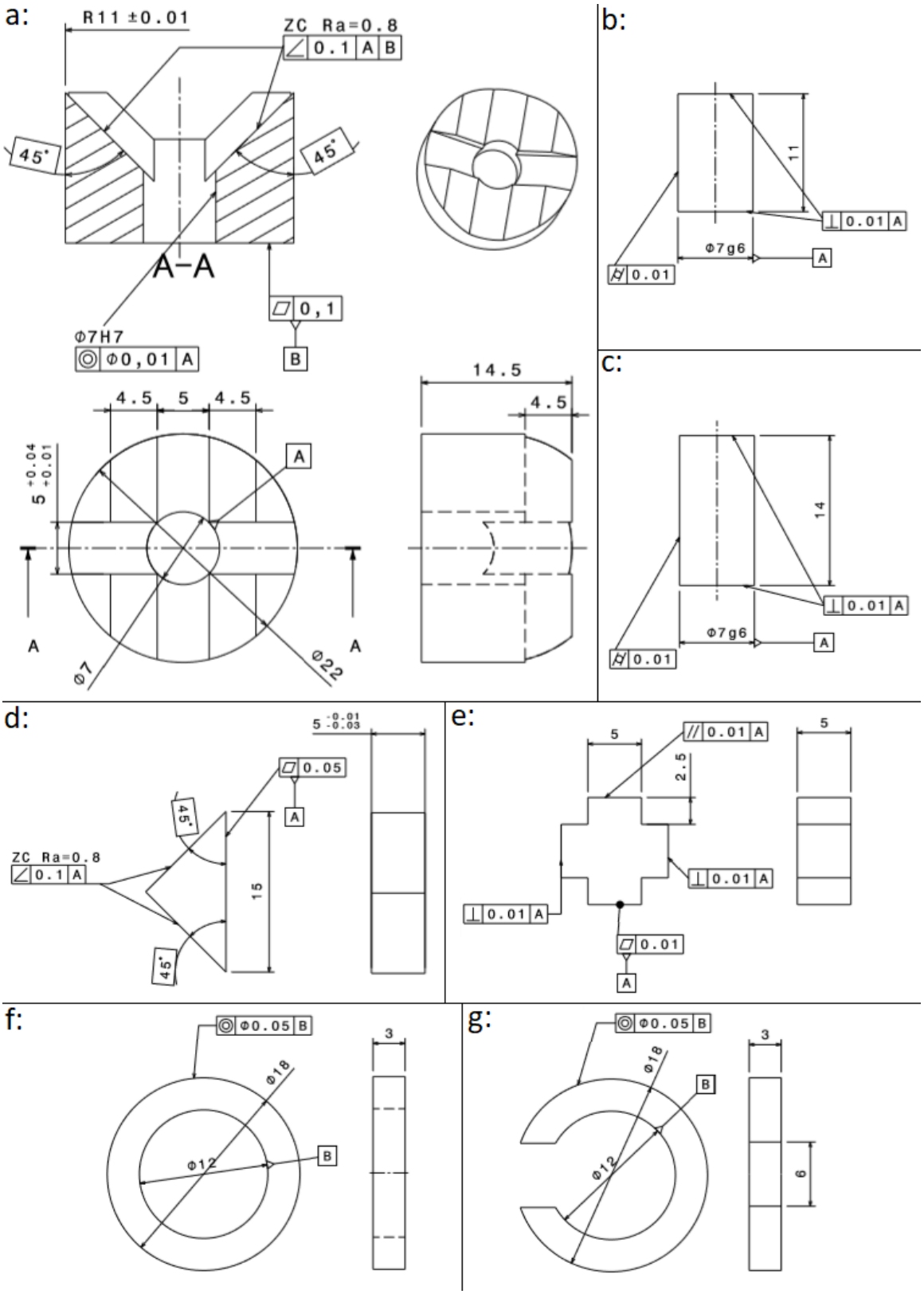

Figure 2: Part drawings (general tolerances: 0.1 mm); a: parts with the sliding surfaces, b: left-hand cylinder, c: right-hand cylinder, d: transverse triangular parts, e: sample, f: bearings, g: opened bearings.

The cylinder noted "b" in Figure 2 is inserted between the input bar and the sample, and the cylinder "c" is inserted between the sample and the internal output bar (see Figure 1). Both cylinders apply the axial loading on the cross sample and the right-hand one in Figure 1 (the "c") is free to have an axial motion relatively to the right-hand part with the sliding surfaces ("a").

2.2 Forces and velocities in the set-up

Strain gauges are glued at the middle of the input bar and on the two output bars close to the sample but far enough from the ends (at 0.374 m on the external bar and at 0.612 m on the internal one) to be within the Saint-Venant conditions.

After the striker impact, the input bar gauge measures an incident compressive wave ε_i followed by a reflected tensile wave ε_r. Moreover, the external output gauge measures a transmitted wave in the external output bar, ε_{et} and the internal output gauge also measures a transmitted wave in the internal output bar, ε_{it}. ε_i can be seen as a loading imposed to the biaxial set-up whereas ε_r, ε_{et} and ε_{it} can be seen as the set-up response to the imposed loading.

These strain waves have to be virtually transported from the gauge positions to the interfaces between the bars and the set-up presented in Figure 1, down. Thus, ε_i has to be delayed and ε_r, ε_{et} and ε_{it} have to be shifted forward of the duration necessary for the waves to propagate from the measurement gauge to the corresponding interface. Then the Hopkinson formulae enable for the determination of the forces and of the velocities at the interfaces from these transported waves and from the bar parameters given in Table 1:

$$F_i = -\rho_i {C_i}^2 \pi {R_i}^2 (\varepsilon_i + \varepsilon_r) \quad (1)$$

$$V_i = C_i(\varepsilon_r - \varepsilon_i) \quad (2)$$

(3) $$F_{eo} = -\rho_{eo} {C_{eo}}^2 \pi \left({R_{eeo}}^2 - {R_{ieo}}^2 \right) \varepsilon_{et}$$

(4) $$V_{eo} = -C_{eo} \varepsilon_{et}$$

(5) $$F_{io} = -\rho_{io} {C_{io}}^2 \pi {R_{io}}^2 \varepsilon_{it}$$

(6) $$V_{io} = -C_{io} \varepsilon_{it}$$

F_i and V_i are the force and the velocity at the interface between the input bar and the set-up shown in Figure 1, F_{eo} and V_{eo} are the force and the velocity at the external output bar interface and F_{io} and V_{io} are the force and the velocity at the internal output bar interface.

Under the assumption of an equilibrium state in the set-up, the axial force in the sample can be assumed to be equal to the internal output force F_{io} and the transverse force F_t can be deduced from the external output force F_{eo}. Indeed, each transverse triangular part of the mechanism is axially submitted to half F_{eo} and by taking account of friction, the mechanical equilibrium of a transverse triangular part leads to Figure 3.

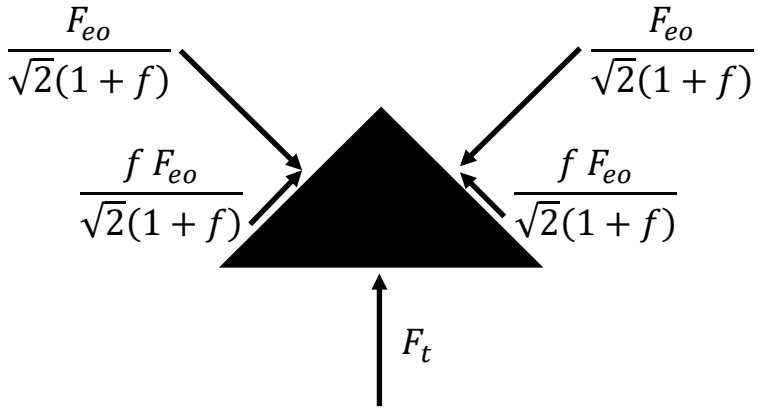

Figure 3: Equilibrium of a transverse triangular part axially submitted to half F_{eo}.

As the Figure 3 upper triangle moves from top to bottom, the applied friction forces are oriented from bottom to top. Besides, according to the Coulomb's laws, the friction force over normal force ratio is imposed to be equal to the friction coefficient at the mechanism sliding interfaces, noted *f*. The axial projection of the force transmitted by a sliding surface corresponds to half F_{eo} (the axially applied force) and the transverse projection corresponds to F_t, which leads to:

$$F_t = \frac{1-f}{1+f} F_{eo} \quad (7)$$

3 Experimental results

3.1 Strain gauge measurement and image processing

Axial strain gauges are glued on each of the three bars and the measurement frequency is 500 kHz. The Hopkinson formulae (equations (1), (3) and (5)) permit for the calculation of the forces at the interfaces between the bars and the set-up from these measurements. The camera trigger signal is measured in the same time-basis as the gauge voltages. The image which was being recorded in the camera at the arrival of the trigger signal being known, both measurements can be time shifted.

The speckled samples are observed during the tests thanks to an SA5 high-speed camera whose frequency is 50 kHz at a definition of 512 pixels × 272 pixels. Images of the samples are acquired during the tests. The first one is called reference image and the displacement between each image and the reference is calculated thanks to Digital Image Correlation (DIC). DIC is performed by using the in-house Correli RT3 software [16], [17]. The displacement field is defined over a finite-element mesh made of triangular 3-noded elements (T3). The chosen element size is 10 pixels. The mean displacements on the four sample interfaces and the resulting axial and transverse elongations are determined from DIC. The displacement is given

in pixels, which are converted into millimeters knowing the sample dimension. In order to control the uncertainty of the DIC calculation, an elastic regularization is used [16], [17].

The relative weight applied to the reference solution can be seen as the fourth power of a length called the regularization length. A too high regularization length may lead to erroneous estimations of the experimental displacement field because this field is thus constrained to be close to an elastic solution. As a result, the DIC calculations are processed with a regularization length decreasing from a value corresponding to 3 times the element size (30 pixels) to a value equal to the element size (10 pixels). DIC gives identical results when the length varies from 30 to 20 pixels but the results obtained with a 10 pixel length are sometimes a bit noisy and slightly different from the previous ones. To reduce the noise, a 20-pixel length is thus chosen for the processing.

3.2 Identification of the sample material behavior

The samples are made of an AW-2017A aluminum. The material stress-strain law is identified from simple compression tests on cuboid samples (5 mm × 5 mm × 10 mm) inserted between the input bar and the internal output bar (the external output bar being removed, see Figure 4a).

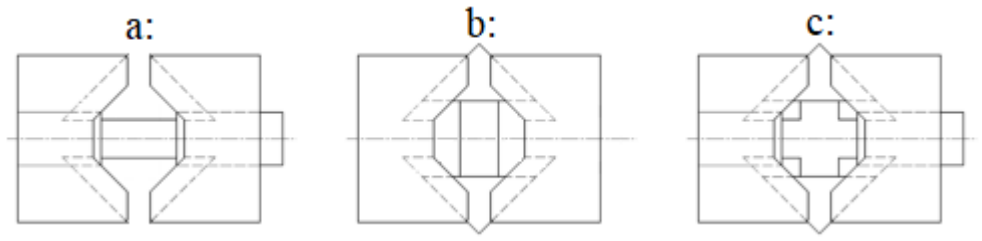

Figure 4: Schematics of the tests; a: cuboid sample axially compressed, b: cuboid sample transversally compressed, c: cross sample bi-axially compressed.

The compression force in the sample (Figure 4, case a) thus corresponds to the internal output force F_{io}. The sample axial and transverse elongations in the image plan are determined from DIC. The real cross section (which increases because of compression), and then the true stress, can thus be calculated. Meanwhile, the axial logarithmic strain is deduced from the corresponding axial elongation. These measurements lead to repeatable axial behaviors.

3.3 Identification of the friction at the mechanism sliding interfaces

The friction coefficient in the mechanism of this new bi-axial testing device is a key parameter which has to be determined under the bi-axial test conditions. In order to reproduce the reached sliding velocities at the sliding interfaces, identical AW-2017A cuboid samples are inserted between the input bar and the external output bar, and are compressed via the mechanism (the internal output bar being removed, see Figure 4b). The ratio between the transverse compression force F_t and the external output force F_{eo} is thus friction dependent according to relation (7).

The set-up being far too small to insert a cell able to measure the compression force in the sample, this force will be deduced from relation (7) and from the F_{eo} measurement. The friction coefficient f will be estimated knowing that the force-elongation laws identified during the axial (Figure 4a) and the transverse (Figure 4b) tests must be the same because the tested cuboid samples are the same too.

According to Figure 5, by multiplying the external output force F_{eo} measured during the transverse test by a constant ratio, a satisfactory fit can be obtained between the transverse and the axial tests when the displacements become high enough. However, for low displacements, the ratio should be a bit lower to obtain a satisfactory fit. It implies that the friction is first higher (adhesion phase) and then decreases when the displacements become high enough (sliding phase), which is finally consistent with the Coulomb's law.

Figure 5 represents typical curves obtained from an axial test and from a transverse one, chosen as average behaviors. The transverse curve shows that the adhesion phase is not stationary, unlike the sliding one. The friction will thus be identified only during the sliding phase. The noise of the transverse force-elongation curve will lead to an uncertainty on the friction. By fitting, in the sliding phase, the transverse curve points with the minimal forces and the axial curve, a lower bound of the friction coefficient is obtained. Inversely, by fitting, in the sliding phase, the transverse curve points with the maximal forces and the axial curve, an upper bound of the coefficient is obtained. One obtains $0.05 < f < 0.09$. Such values are consistent with Vaseline lubricated interfaces. It finally leads to a 0.87 average F_t/F_{eo} ratio with a 4 % relative uncertainty.

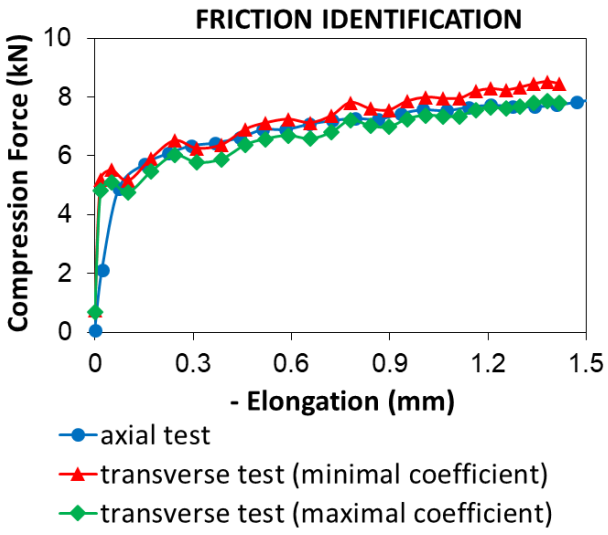

Figure 5: Friction identification by fitting the transverse test and the axial one.

The friction coefficient magnitude and the corresponding uncertainty knowledge does not matter in itself, but it will enable for the determination of the transverse force and of the corresponding uncertainty during the bi-axial test.

Without clearances and without intermediate strains in the set-up, the corresponding interface sliding velocity should be equal to the difference between the input velocity and the

external output one, or to the opposite of the transverse sample elongation rate, both divided by $\sqrt{2}$ (because of the 45° angle):

$$V_{int,bars} = \frac{V_i - V_{eo}}{\sqrt{2}} \quad (8)$$

$$V_{int,sample}(t) = \frac{\Delta l(t-\Delta t) - \Delta l(t+\Delta t)}{2\sqrt{2}\,\Delta t} \quad (9)$$

$V_{int,bars}$ is the interface sliding velocity estimated from the bar interface velocities (relations (2) and (4)) whereas $V_{int,sample}$ is the same quantity estimated from the sample elongation Δl. Formula (9) corresponds to a numerical differentiation, t being a measurement instant and Δt the elongation acquisition time (given by the camera).

These velocity estimations show that a stationary phase with an interface sliding velocity of around 1 to 3 m/s begins for an elongation of approximately 0.1 mm, which is consistent with the beginning of the phase with a constant friction identified in Figure 5.

3.4 Analysis of the bi-axial test measurements

An AW-2017A cross sample is tested by using the whole bi-axial mechanism and the two output bars (see Figure 1 or Figure 4c). The forces applied by the bars on the bi-axial set-up are determined from the strain gauge measurements and from the Hopkinson formulae and are shown in Figure 6.

Figure 6 shows that the input force and the total output force are in satisfactory equilibrium, despite of the complex 3-dimensionnal wave propagation phenomena occurring in the bi-axial mechanism. According to Section 2.2, the axial compression force in the sample corresponds to F_{io} whereas the transverse compression force F_t is lower than F_{eo} but almost equal because of the low friction (in Section 3.3, the estimated F_t/F_{eo} ratio is roughly 0.87). The

obtained transverse and axial forces (F_t and F_{io}) being very close, Figure 6 thus displays that the force loading path in the sample is rather equi-bi-axial.

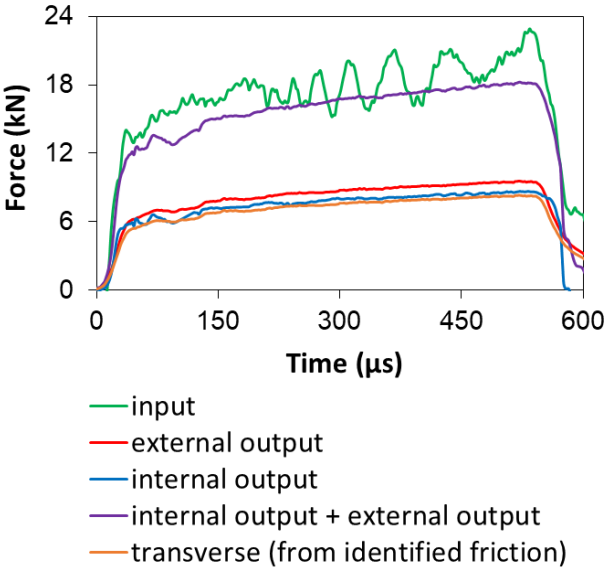

Figure 6: Time evolutions of the forces at the interfaces.

As the external and the internal output bars have nearly the same impedance, the velocities, and thus the displacements, at the external and the internal output bar boundaries are also very similar. If there were no clearances and no strains occurring in the mechanism intermediate parts, the transverse displacement of each of the two triangular parts would be half the difference between the input bar and the external output bar displacements. The triangular parts moving symmetrically, the sample elongations, in both directions, would thus be exactly equal to the difference between the displacements at the input bar and at the output bar interfaces. It displays that the elongation loading path may be also rather equi-bi-axial.

The cross sample axial and transverse elongations are determined from the images and from DIC. The DIC reference image and the corresponding meshes on the sample are shown in Figure 7.

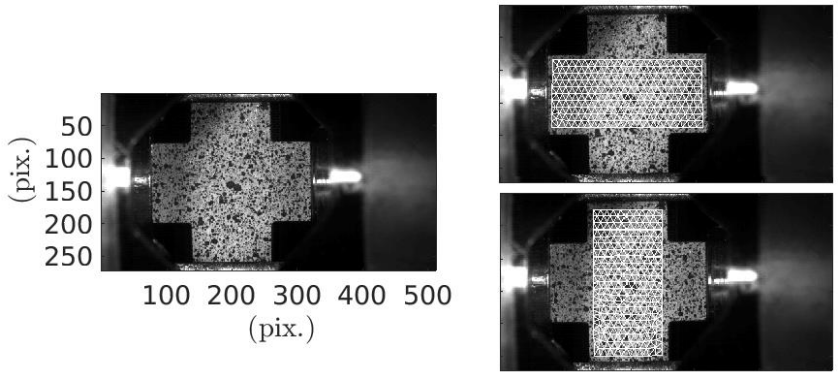

259

260 Figure 7: Reference image (left), mesh used to determine the axial displacements (right, up)

261 and mesh used to determine the transverse displacements (right, down).

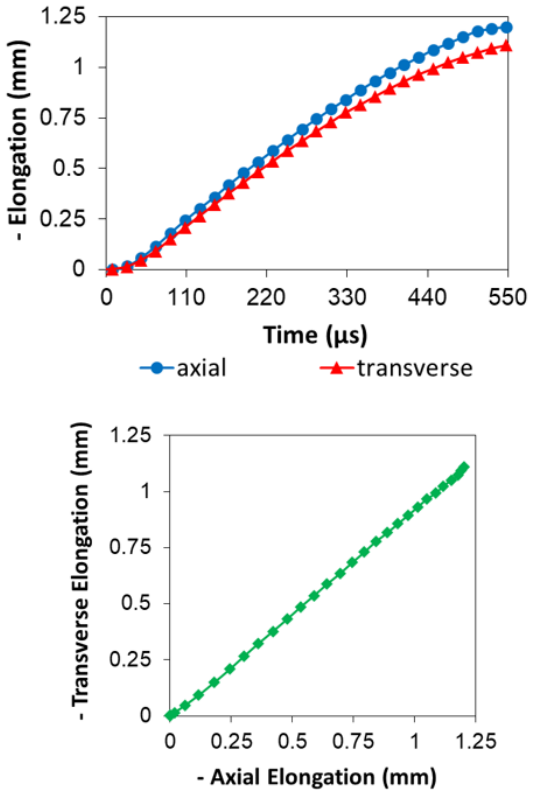

262

263 Figure 8: Time-evolutions of (the opposite of) the elongations in both directions (up) and

264 corresponding loading path (down).

265 The obtained elongation time-evolutions and the corresponding transverse-axial loading

266 path can be seen in Figure 8, which clearly confirms that an almost equi-bi-axial loading is

imposed to the sample. This bi-axial state can also be seen in Figure 9, which also shows the set-up capacities in both directions.

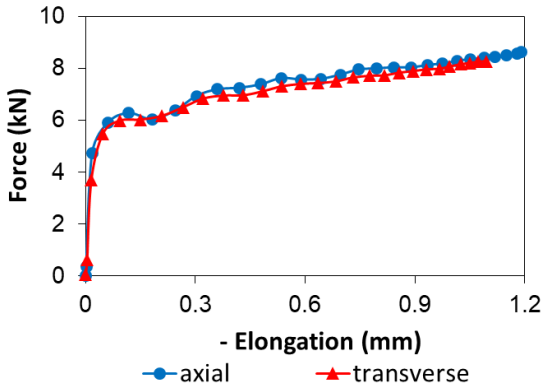

Figure 9: Sample force-elongation curves in axial and transverse directions.

Formulae (8) and (9) show that the sliding velocity reached at the interface during the stationary phase is of the order of 1 to 3 m/s, like during the friction identification test. It confirms the relevance of the friction coefficient value used for data processing.

4 Check of the measurement consistency thanks to simulations

4.1 Material modelling

A typical result obtained from an axial compression test on a cuboidal sample (Figure 4a), and chosen as a reference is reported in Figure 10.

As there are few measurement points in the elastic phase, a 70 GPa Young modulus and a 0.3 Poisson's ratio are assumed (AW-2017A characteristics). A yield stress - plastic strain law with a 100 MPa elastic threshold, and which exactly fits the measurements is then chosen (see retained behavior in Figure 10). To simplify the modelling, the stress is supposed to saturate at a 268 MPa threshold value, which also well fits the measurements. In practice, the axial curves are reproducible for strains lower than 3 %, but a 4 % dispersion is observed for

the threshold value. These parameters are implemented in a Von-Mises elastic-plastic model with an isotropic hardening. The used software is ABAQUS.

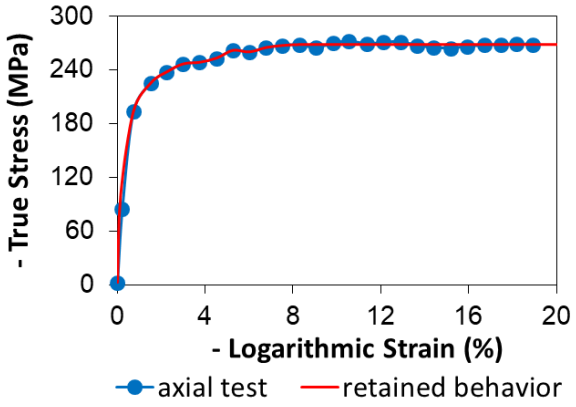

Figure 10: Stress-strain law identified from a test.

4.2 Simulation of the sample behavior

Because of its cross-shape, the stress and the strain states in this sample are heterogeneous. So, to check the force and elongation measurement consistency, a finite-element simulation must be performed. The calculations are performed with the Figure 10 retained behavior. The fact that the model identification test has been carried out in the same dynamic conditions as the bi-axial test implies that the method remains valid with a strain rate dependent behavior. If any contact occurs between the arm free boundaries, it will be supposed frictionless. According to Figure 6, the bi-axial set-up, and therefore the cross sample, are in a satisfactory equilibrium. This equilibrium state can be accurately verified by processing a dynamic explicit calculation. The chosen density is 2800 $kg.m^{-3}$.

The displacements estimated thanks to DIC calculations are directly imposed to the sample interfaces (Figure 11). Because of the image plan symmetry, only half the sample has to be modelled (Figure 12). 8-node linear brick elements are used. The chosen brick size is 0.25 mm, which leads to the Figure 12 mesh.

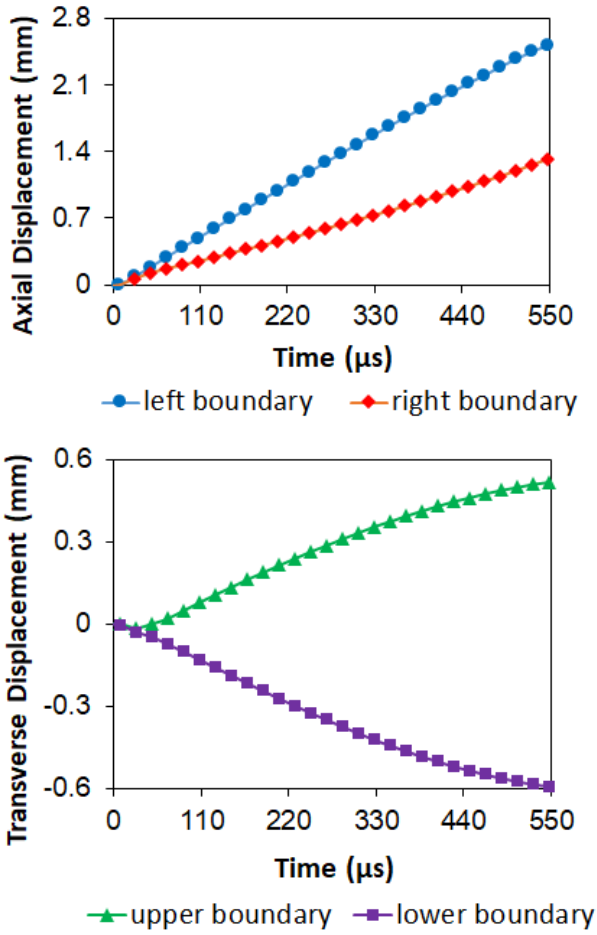

302

303 Figure 11: Imposed boundary displacements (axial ones oriented from left to right and
304 transverse ones oriented from top to bottom).

305 The dynamic explicit calculations display that the forces applied at opposite boundaries
306 are almost equal until 60 µs, and become exactly the same after this duration. The sample
307 equilibrium assumption being checked, the axial force is defined as the left and right boundary
308 force average and the transverse force as the upper and lower boundary force average.

309 The numerical and the experimental forces in both directions can then be compared to
310 check the measurement consistency. Because of the behavior dispersion (see Section 4.1), a
311 4 % relative uncertainty must be considered for the numerical forces. The friction is taken into
312 account by determining the measured transverse force with the 0.87 estimated F_t/F_{eo} ratio (see
313 end of section 3.3). The 4 % relative uncertainty of this ratio also leads to a 4 % uncertainty of

the measured transverse force. It could be noted that the uncertainty due to friction is not so high.

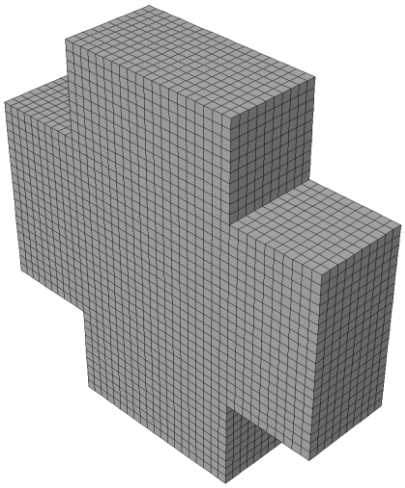

Figure 12: Meshed sample model accounting of the symmetry plan.

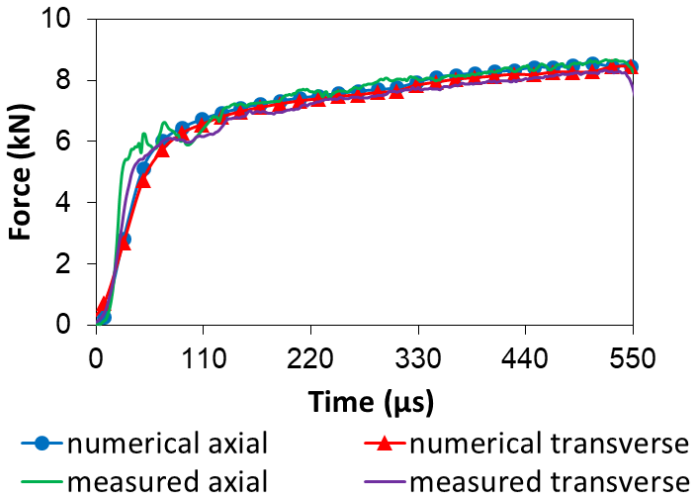

Figure 13: Comparison between the experimental forces and the numerical forces obtained from the measured displacements and from the identified model.

In Figure 13, the numerical forces are obtained at the displacement measurement frequency (i.e. every 20 µs). As expected, the fit is not perfect at the very beginning of the test because of the following reasons:

- These is a too weak number of acquisition points in the elastic phase to accurately measure the brutal increase of the forces.
- The sample equilibrium being not perfect during the first 60 µs, the axial and the transverse forces in the cross sample do not exactly correspond to measured forces at the output bar interfaces (i.e. F_{io} and F_{eo} multiplied by the friction dependent ratio).
- The transverse force is determined from the sliding friction coefficient, and as explained in section 3.3, this method overestimates the force at the very beginning of the test, i.e. in the adhesion phase.

However, during the stationary phase, the measurement consistency is clearly proven. It validates the identified sample model. Although this processing is not performed to measure the friction, it also shows that the friction coefficient used to process the data is consistent.

4.3 Simulation of the whole apparatus behavior

The axial and transverse forces in the sample are both determined from the forces at the interfaces between the output bars and the set-up. This determination is based on the equilibrium assumption, which actually implies a quick enough transmission of the wave through the mechanism. A satisfactory, but not perfect, equilibrium is experimentally shown in Figure 6. However, the incident strain wave ε_i and the reflected one ε_r being rather opposite, as shown in Figure 15, the input force F_i determination from formula (1) is very noise sensitive. A simulation of the whole bar set-up has thus been performed to study this equilibrium. The used software is still ABAQUS in its explicit version.

The aluminum sample is supposed to have the properties given in Sections 4.1 and 4.2. The bi-axial mechanism parts are supposed to be made of the input bar steel (it is actually the case) whose Poisson's ratio is 0.3 (density and wave celerity given in Table 1), and to remain purely elastic. The same assumptions are used to model the output bars (densities and wave

348 celerities also given in Table 1). The striker initial velocity is 6 $m.s^{-1}$, which is consistent with
349 experimental measurements (Figure 15). The selected friction coefficient at the contact surfaces
350 is 0.07, as measured in Section 3.3. The static and the dynamic coefficients are supposed to be
351 the same.

352 Because of the two symmetry planes (the cutting plane in Figure 1 and the one normal
353 to the section plane and containing the axis), only a quarter of the system is studied. The bars
354 and the projectile are modelled by 6-node linear triangular prism elements (ABAQUS
355 terminology) whose approximate size is 5 mm. The two parts with the sliding surfaces and the
356 tubes inserted between the sample and the input bar and between the sample and the internal
357 output bar are modelled by the same elements but their rough sizes are respectively 10 mm and
358 2.5 mm. The triangular part is composed of two triangular prism elements separated by the
359 symmetry plane. The sample is merely composed of four 8-node linear brick elements: one
360 corresponding to the center and three corresponding to the three arms represented in the
361 simplified model. As shown in Figure 15, element sizes are thin enough to roughly fit the
362 measurements. The chosen time increment is 0.1 μs.

363 The experimental results display that the contacts in the bi-axial mechanism are not
364 perfect. In Figure 14, a non-negligible gap can be seen between the sample elongations and the
365 differences between the input and the output bar displacements. As explained in Section 3.4,
366 these quantities would be identical if there was neither clearances nor intermediate strains. The
367 numerical equivalent of this gap is lower, and only due to the elastic strains of the mechanism
368 parts. It implies that the numerical set-up is a little bit stiffer than the real one. However, the
369 stiffness remaining in the same order, it enables to check the general relevance of the set-up.

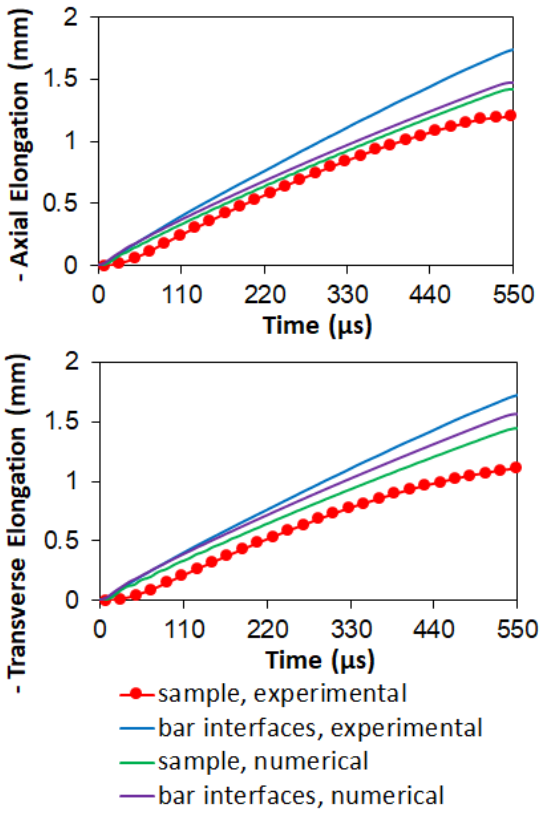

370

371 Figure 14: Comparisons between the sample elongations and the differences between the bar

372 displacements.

373 The gauges are glued at the middle of the input bar and on the two output bars at 0.374 m

374 from the interface with the set-up on the external bar, and at 0.612 m on the internal one. The

375 experimental and the numerical strain time-evolutions are compared in Figure 15. The input

376 gauge first measures the incident wave ε_i, and then the reflected wave ε_r. The external output

377 gauge and the internal one measure the external transmitted wave ε_{et} and the internal transmitted

378 wave ε_{it}. ε_i can be seen as a loading imposed to the bi-axial set-up whereas ε_r, ε_{et} and ε_{it} can be

379 seen as the set-up response to the imposed loading. Figure 15 shows that the simulated ε_i

380 (proportional to the striker initial velocity) rather fits the experimental one, despite some

381 spurious oscillations. The numerical transmitted waves are a little bit higher than the

382 experimental ones, which is fully consistent with a modelled set-up stiffer than the real one.

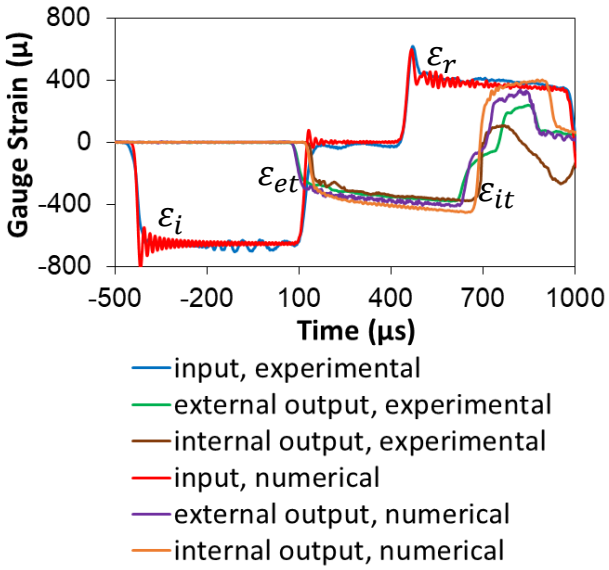

383

384 Figure 15: Experimental and numerical strain time evolutions at the gauge positions.

385 Figure 16 finally shows that, in spite of numerical oscillations, the input force and the
386 total output force are in mean equilibrium and that both output forces are the same.

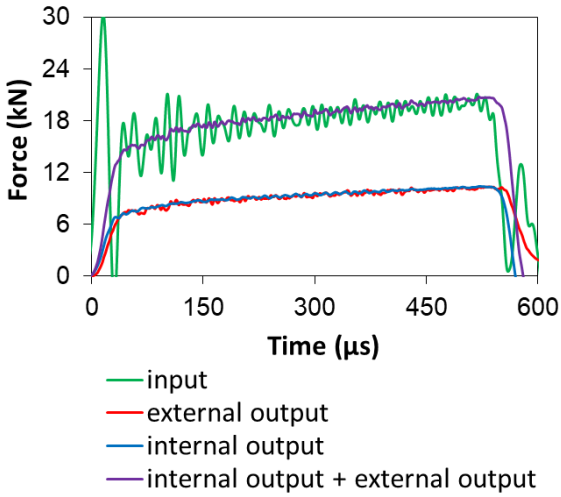

387

388 Figure 16: Time evolutions of the numerical forces at the interfaces.

389 The finite element mesh can be seen in Figure 17. As the contacts are not perfectly
390 modeled, using a smaller mesh would be useless to better fit the measurements.

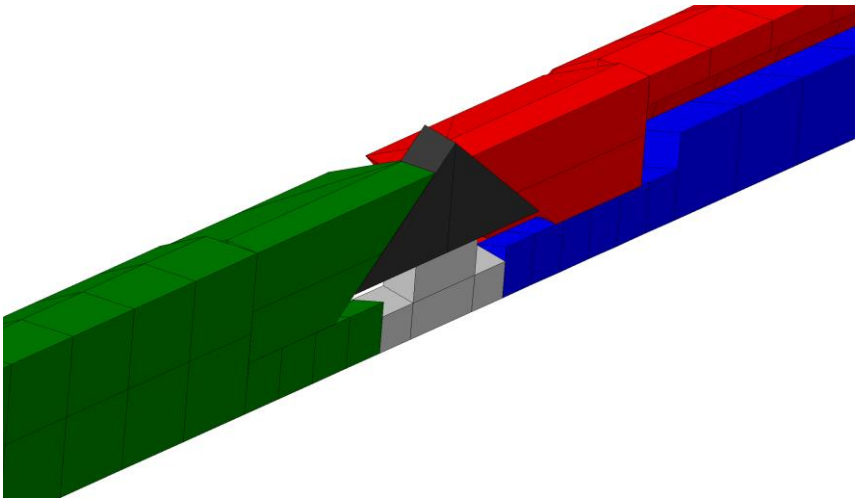

Figure 17: Finite element mesh.

5 Conclusion

The aim of the study was to check the relevance of a newly designed Hopkinson bi-axial compression set-up. The sample axial compression is directly generated by an internal output bar whereas the transverse compression is indirectly generated by an external output bar via a mechanism. The friction in the mechanism is identified in the relevant dynamic conditions from comparisons between axial and transverse compression tests on cuboid samples. To reproduce the sliding velocities reached at the mechanism sliding interfaces during the bi-axial test, these cuboid samples are made of the bi-axial sample material. The friction being identified, any sample can now be tested.

A calibration bi-axial test has been performed on a cross sample with a simple shape, and therefore easy to model. The measurements show that the device ensures an approximate equality between the axial and the transverse loadings, and the experimental result reliability is proven by a numerical modelling of the bi-axial sample. The set-up can therefore be used in the future for characterization on more complex samples and materials (which was not the aim of this first study).

Finally, the design of an easily buildable set-up generating and measuring a rather isotropic dynamic bi-axial loading has been achieved.

Conflict of Interest

The authors declare that they have no conflict of interest.

6 References

[1]: **L. Durrenberger**. Analyse de la pré-déformation plastique sur la tenue au crash d'une structure crash-box par approches expérimentale et numérique. *PhD Report, Paul VERLAINE University of Metz (2007).* In French.

[2]: **W. Liu**. Identification of strain rate dependent hardening sensitivity of metallic sheets under in-plane biaxial loading. *PhD Report, INSA de Rennes (2015).*

[3]: **Y. Guo, M. Efe, W. Moscoso, D. Sagapuram, K.P. Trumble, S. Chandrasekar**. Deformation field in large-strain extrusion machining and implications for deformation processing. *Scripta Materialia, 66, 235-238 (2012).*

[4]: **W. Chen, B. Song**. Split Hopkinson (Kolsky) Bar. Design, Testing and Applications. *Springer Science & Business Media, LLC (2011).*

[5]: **B. Durand, F. Delvare, P. Bailly, D. Picart**. A split Hopkinson pressure bar device to carry out confined friction tests under high pressures. *International Journal of Impact Engineering, 88, 54-60 (2016).*

[6]: **P. Bailly, F. Delvare, J. Vial, J.L. Hanus, M. Biessy, D. Picart**. Dynamic behavior of an aggregate material at simultaneous high pressure and strain rate: SHPB triaxial tests. *International Journal of Impact Engineering, 38, 73-84 (2011).*

[7]: **C. Albertini, E. Cadoni, G. Solomos**. Advances in the Hopkinson bar testing of irradiated/non-irradiated nuclear materials and large specimens. *Philosophical transactions of the Royal Society A. Mathematical, physical and engineering sciences, 372, 2015 (2014).*

[8]: **D. Rittel, S. Lee, G. Ravichandran**. A shear-compression specimen for large strain testing. *Experimental Mechanics, 42(1), 58-64 (2002).*

[9]: **B. Hou, A. Ono, S. Abdennadher, S. Pattofatto, Y.L. Li, H. Zhao**. Impact behavior of honeycombs under combined shear-compression. Part I: Experiments. *International Journal of Solids and Structures, 48(5), 687-697 (2011).*

[10]: **J.L. Lewis, W. Goldsmith**. A Biaxial Split Hopkinson Bar for Simultaneous Torsion and Compression. *Review of Scientific Instruments, 44(811) (1973).*

[11]: **K. Stiebler, H.D. Kunze, E. El-Magd**. Description of the flow behavior of a high strength austenitic steel under biaxial loading by a constitutive equation. *Nuclear Engineering and Design, 127, 85-93 (1991).*

[12]: **S. Philippon, G.Z. Voyiadjis, L. Faure, A. Lodygowski, A. Rusinek, P. Chevrier, E. Dossou**. A Device Enhancement for the Dry Sliding Friction Coefficient Measurement Between Steel 1080 and VascoMax with Respect to Surface Roughness Changes. *Experimental Mechanics, 51(3), 337-358 (2011).*

[13]: **C. Albertini, M. Montagnani**. Dynamic Uniaxial and Biaxial Stress-Strain Relationships for Austenitic Stainless Steels. *Nuclear Engineering and Design, 57, 107-123 (1980).*

[14]: **A. Hummeltenberg, M. Curbach**. Entwurf und Aufbau eines zweiaxialen Split-Hopkinson-Bars. *Beton- und Stahlbetonbau, 107(5) (2012).* In German.

[15]: **V. Grolleau, G. Gary, D. Mohr**. Biaxial Testing of Sheet Materials at High Strain Rates Using Viscoelastic Bars. *Experimental Mechanics, 48, 293–306 (2008).*

[16]: **S. Roux, F. Hild, H. Leclerc**. Mechanical Assistance to DIC. Proceedings of Full-Field Measurements and Identification in Solid Mechanics. *F. Hild and H. Espinosa eds., Procedia IUTAM 4, 159-168, Elsevier, (2012).*

[17]: **Z. Tomicevc, F. Hild, S. Roux**. Mechanics-aided digital image correlation. *Journal of Strain Analysis, 48(5), 330-343 (2013).*

Acknowledgments

The authors thank their colleague F. Hild for his advice, which helped to improve the article.